A&A 453, 1117-1127 (2006)
DOI: 10.1051/0004-6361:20054768

https://www.aanda.org/articles/aa/full/2006/27/aa4768-05/aa4768-05.right.html

Two-dimensional spectroscopy of a sunspot*

III. Thermal and kinematic structure of the penumbra at 0.″5 resolution

L. R. Bellot Rubio[1,2] - R. Schlichenmaier[2] - A. Tritschler[3,2]

1 - Instituto de Astrofísica de Andalucía (CSIC), Apdo. 3004, 18080 Granada, Spain
2 - Kiepenheuer-Institut für Sonnenphysik, Schöneckstr. 6, 79104 Freiburg, Germany
3 - National Solar Observatory/Sacramento Peak**, PO Box 62, Sunspot, NM 88349, USA

Received 23 December 2005 / Accepted 28 March 2006

Abstract
We investigate the thermal and kinematic configuration of a sunspot penumbra using high spectral and spatial resolution intensity profiles of the non-magnetic Fe I 557.6 nm line. The data set was acquired with the 2D solar spectrometer TESOS. The profiles are inverted using a one-component model atmosphere with gradients of the physical quantities. From this inversion we obtain the stratification with depth of temperature, line-of-sight velocity, and microturbulence across the penumbra. Our results suggest that the physical mechanism(s) responsible for the penumbral filaments operate preferentially in the lower photosphere. The spot, located at an heliocentric angle of 23°, exhibits larger continuum intensities in the center-side penumbra as compared with the limb side, which translates into an average temperature difference of 100-150 K at $\log\tau_{500} = 0$. We investigate the nature of the bright ring that appears in the inner penumbra when sunspots are observed in the wing of spectral lines. It is suggested that the bright ring does not reflect a temperature enhancement in the mid photospheric layers. The line-of-sight velocities retrieved from the inversion are used to determine the flow geometry at different heights in the photosphere. Both the flow speed and flow angle increase with optical depth and radial distance. Downflows are detected in the mid and outer penumbra, but only in deep layers ($\log\tau_{500} \geq -1.4$). We demonstrate that the velocity stratifications retrieved from the inversion are consistent with the idea of penumbral flux tubes channeling the Evershed flow. Finally, we show that larger Evershed flows are associated with brighter continuum intensities in the inner center-side penumbra. Dark structures, however, are also associated with significant Evershed flows. This leads us to suggest that the bright and dark filaments seen at 0.″5 resolution are not individual flow channels, but a collection of them. Our analysis highlights the importance of very high spatial resolution spectroscopic and spectropolarimetric measurements for a better understanding of sunspot penumbrae.

Key words: line: profiles - Sun: photosphere - sunspots

1 Introduction

The fine structure of the penumbra is intimately connected to the Evershed flow, the most conspicuous dynamical phenomenon observed in sunspots (e.g., Solanki 2003; Thomas & Weiss 2004). Therefore, a proper observational characterization of this fine structure is essential to understand the Evershed flow and, more generally, the nature of the penumbra itself.

Studying the penumbra is difficult because of the very small scales involved. Recent imaging observations with the Swedish 1-m Solar Telescope (Scharmer et al. 2002; Rouppe van der Voort et al. 2004) have revealed that

even at a resolution of 0.″1 some of the filaments that form the penumbra may be unresolved. That is, different structures (each having different properties) may coexist in the resolution element, and we are not able to separate them. A proper characterization of the penumbra calls not only for diffraction-limited imaging observations, but also for more quantitative spectroscopic and spectropolarimetric analyses at the highest resolution possible. By interpreting the shape of spectral lines we can derive the thermal, magnetic, and kinematic configuration of the penumbra via the Zeeman and Doppler effects. Unfortunately, current spectroscopic observations do not attain resolutions better than $\sim 0.''5$, and this limit is often reached at the cost of poor spectral resolution. The situation is even worse in the case of spectropolarimetric measurements: the best angular resolution of existing solar polarimeters is about 0.″7-0.″8.

This paper is the third of a series devoted to the analysis of 2D spectroscopic observations of a sunspot. The data were acquired with the TElecentric SOlar Spectrometer (TESOS, Kentischer et al. 1998; Tritschler et al. 2002) and the Kiepenheuer Adaptive Optics System (KAOS, Soltau et al. 2002; von der Lühe et al. 2003) at the German Vacuum Tower Telescope of Observatorio del Teide (Tenerife, Spain). These observations combine high spectral ($\lambda/\Delta\lambda \sim 250\,000$) and spatial (0.″5) resolution (Tritschler et al. 2004, hereafter referred to as Paper I). In Paper II of this series (Schlichenmaier et al. 2004), we investigated the properties of the Evershed flow through a bisector analysis of the observed intensity profiles.

Here we perform a full inversion of the same data set in order to study the thermal and kinematic configuration of the penumbra. Our analysis allows us to explain a number of findings reported in Paper I and to remove some of the uncertainties associated with the methods employed in Paper II. At the same time, we gather new information on the thermal properties of the penumbra. This is particularly important because very few thermal studies of sunspot penumbrae have been published to date (del Toro Iniesta et al. 1994; Balasubramaniam 2002; Rouppe van der Voort 2002; Sánchez Cuberes et al. 2005).

A brief account of the observations and the inversion procedure is given in Sect. 2. In Sect. 3 we discuss the maps of physical quantities inferred from the inversion. The thermal and kinematic structure of the penumbra is studied in Sects. 3.1 and 3.2. Some implications of the results are presented in Sect. 4, and a summary of our findings is given in Sect. 5.

2 Observations and data analysis

On July 5, 2002, TESOS was used to measure the intensity profiles of Fe I 557.6 nm in the main sunspot of NOAA AR 10019 (cf. Paper I). The spot was located 23° off the disk center (heliographic coordinates W4 S17). The line was scanned at 100 wavelength positions with a wavelength step of 8.4 pm, corresponding to overcritical spectral sampling. The time needed to complete the scan was 37 s. The KAOS system provided real-time correction of wavefront distortions due to turbulence in the Earth's atmosphere. Operated in high resolution mode, TESOS yielded a pixel size of $0.''089 \times 0.''089$. The filtergrams have been binned by a factor of 2 to improve the signal-to-noise ratio. The increased pixel size is still sufficient to sample our seeing-limited spatial resolution of about 0.″5. After binning, 37 000 individual profiles are left for analysis.

Fe I 557.6 nm is a fairly strong photospheric line with zero effective Landé factor (g=0). The diagnostic capabilities of this line are investigated in Appendix A. There we show that, contrary to commonly held views, Fe I 557.6 nm is one of the most temperature-sensitive lines used in solar physics.

The intensity profiles have been inverted in order to determine the stratification of temperature, line-of-sight (LOS) velocity, and microturbulence with optical depth. To this end, we have used the SIR code (Ruiz Cobo & del Toro Iniesta 1992). Despite the high spectral resolution of our observations, the number of data points does not allow us to determine complex atmospheric models. Hence, we have adopted a simple one-component model with gradients of the physical parameters.

We derive the temperature stratification by modifying the thermal structure of the penumbral model of del Toro Iniesta et al. (1994; hereafter TTR) with two nodes. For a better recovery of this parameter, the observed profiles are normalized to the continuum intensity of the average quiet sun profile. Such an absolute normalization implies that the continuum of the individual profiles carries information about the temperature in the deep atmospheric layers. The two nodes used to infer the thermal structure allow for changes in the gradient and absolute position [e.g., $T(\tau_{500} = 1)$] of the initial temperature stratification. We assume local thermodynamical equilibrium (LTE). Since non-LTE effects may be important in the upper layers, our temperatures are reliable only up to, say, $\log \tau_{500} \sim -3$. Electron pressures are computed from the inferred temperatures using the equation of hydrostatic equilibrium and the ideal gas law.

The inversion also yields the stratification with depth of the LOS velocity and microturbulent velocity. In both cases we assume linear variations with $\log \tau_{500}$, i.e., two nodes for each parameter. In the case of the LOS velocity, this choice seems to be appropriate considering that most observed bisectors possess quite linear shapes (Paper II). From the inversion we also determine the (height-independent) macroturbulence needed to reproduce the observed line widths. The synthetic profiles are convolved with the instrumental profile of TESOS before being compared with the observed ones. To describe the broadening of the line due to collisions with neutral hydrogen atoms we use the formulation of Anstee, Barklem, & O'Mara (see Barklem et al. 2000). The total number of free parameters is 7, which compares favorably with the number of observables (100).

Further details on the model atmosphere, as well as examples of observed and best-fit profiles, are given in Appendix B.

3 Results

Figure 1 displays the inversion results for the temperature (left panels) and the LOS velocity (middle panels) at two representative optical depths in the atmosphere ($\log \tau_{500} = 0$ and -2). The fine structure of the penumbra is apparent in the deep photosphere, where hot penumbral filaments and flow filaments are seen to extend from the inner to the outer penumbral boundary. The fluctuations in temperature and LOS velocity are much reduced at $\log \tau_{500} = -2$; indeed, no fine-scale organization of the penumbra is obvious at this optical depth. Consequently, the physical mechanisms producing the filaments must operate preferentially in the deep layers.

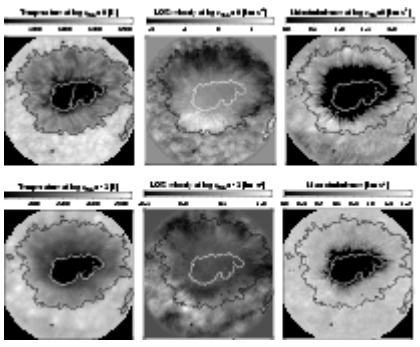

Figure 1: Maps of physical quantities at $\log \tau_{500} = 0$ (*top*) and $\log \tau_{500} = -2$ (*bottom*). Depicted from left to right are the temperature, the LOS velocity and the microturbulence. In this figure, negative LOS velocities indicate redshifts. The lower right panel displays the macroturbulent velocity, assumed to be height independent. Contours outline the inner and outer penumbral boundaries. The arrow points to disk center.

Open with DEXTER

The right panels of Fig. 1 show maps of the microturbulence at $\log \tau_{500} = 0$ and the macroturbulent velocity. According to our results, no microturbulence is needed in either the umbra or the inner penumbra. This is in contrast to the outer penumbra, where microturbulent velocities of 1.8-2 km s^{-1} are common. Thus, the smaller line widths observed in the inner penumbra (Fig. 5 of Paper I) can be interpreted as being due to a reduced microturbulence. Note that the map of microturbulence shows fine structure in the mid penumbra. Also

important is the fact that microturbulence decreases with height, until zero values are reached in high layers (see Sect. 3.2.3). Again, this is consistent with the idea that the mechanisms enhancing the line width operate preferentially in deep atmospheric layers. The macroturbulence stays relatively constant across the penumbra, with values of 1-1.2 km s^{-1}. Only in the very inner penumbra and the umbra is the macroturbulence reduced, perhaps as a consequence of their stronger magnetic fields.

In the next sections, we describe in more detail the thermal and kinematic configuration of the penumbra deduced from the inversion.

3.1 Thermal structure

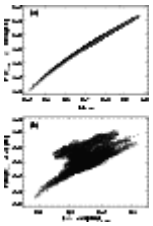

Figure 2: a) Temperature at $\tau_{557.6} = \cos\theta = 0.92$ inferred from the inversion vs continuum intensity (normalized to the continuum of the average quiet sun profile). The solid line represents the temperatures obtained from the Eddington-Barbier approximation using the observed continuum intensities. **b)** Temperature at $\log\tau_{500} = -1.3$ vs. the intensity observed at $\Delta\lambda = -5.2$ pm from line center, normalized to the continuum of the average quiet sun profile.

Open with DEXTER

First, let us examine the reliability of the inferred temperatures. Figure 2a shows the temperature at $\tau_{557.6} = \cos\theta = 0.92$ returned by the inversion code versus the observed continuum intensities. The scatter of the points is small, indicating an excellent correlation between the two quantities. The fact that we use an absolute normalization for the observed profiles is one of the main reasons why the inversion code is able to determine the temperature of the continuum-forming layers so accurately.

The solid line in Fig. 2a represents the temperatures obtained from the Eddington-Barbier approximation $I_\lambda(\theta) = S_\lambda(\tau_\lambda = \cos\theta)$, where $I_\lambda(\theta)$ is the specific intensity observed at an heliocentric angle θ, S_λ the source function (assumed to be the Planck function), and τ_λ the continuum optical depth at the wavelength of the observation. As can be seen, the Eddington-Barbier approximation yields the same temperatures as those deduced from the inversion. Only for small continuum intensities are the inferred temperatures slightly larger than those indicated by the Eddington-Barbier relation, but overall the agreement is very satisfactory. This implies that the observed continuum intensities can be reliably used to estimate temperatures in deep photospheric layers. A similar conclusion has been reached by TTR and Rouppe van der Voort (2002).

In the line wing, the one-to-one correspondence between specific intensity and temperature found before does not hold any longer. This is demonstrated in Fig. 2b, where we plot the temperatures resulting from the inversion at $\log\tau_{500} = -1.3$ versus the intensities observed at -5.2 pm from line center. We use $\log\tau_{500} = -1.3$ because this is the optical depth of the centroid of the contribution function for the line depression at $\Delta\lambda = -5.2$ pm, evaluated in the mean penumbral model atmosphere. It is immediately apparent from the figure that the same line wing intensity can be associated with a wide range of temperatures (up to about 500 K). Thus, line wing intensities cannot be employed to infer temperatures directly. The reason is that the intensities critically depend on the line asymmetries induced by the Evershed flow and on the line width variations due to microturbulent and macroturbulent velocities. All these factors contribute to the large scatter of the points seen in Fig. 2b. The problem has been recognized by Balasubramaniam (2002). In an attempt to cure it, Balasubramaniam introduced the concept of *flowless maps*, i.e., intensity maps constructed by removing the global Doppler shift of the lines emerging from each individual pixel. Unfortunately, flowless maps are still affected by the line asymmetries caused by the Evershed flow.

Let us now investigate the radial variation of the temperature at different optical depths. To this end, we have computed azimuthally averaged temperatures along elliptical paths centered on the spot (cf. Fig. 6 of Paper I). The average temperatures are plotted in Fig. 3 for four optical depths. At all heights in the atmosphere, the temperature is observed to increase radially from the sunspot center to the outer penumbral boundary. This increase is rather linear except for an obvious hump in the inner penumbra, where the temperature seems to be enhanced by several hundreds K. The amplitude of the hump decreases as one moves towards the upper photospheric layers. In deep layers ($\log \tau_{500} = 0$), the hump is so pronounced that the radial variation of the temperature is almost flat between 0.6 and 0.9 penumbral radii (i.e., the mid penumbra and most of the outer penumbra). We also note that the hump is located increasingly closer to the umbra/penumbra boundary as the upper layers are approached. These temperature enhancements could be due to the presence of hot penumbral tubes, as suggested by the numerical simulations of Schlichenmaier et al. (1998). The hot tubes would be more easily detected in the inner penumbra because the plasma emerging from subphotospheric layers quickly cools off by radiation away from the tube's inner footpoint (Schlichenmaier et al. 1999). If the humps exhibited by the temperature curves of Fig. 3 are indeed produced by hot flux tubes, then it is clear that they must be located preferentially in the lower layers.

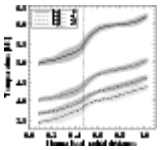

Figure 3: Radial variation of the azimuthally averaged temperatures at different optical depths. The shaded areas represent the standard deviation of the temperatures at each radial distance. The vertical line marks the inner penumbral boundary.

Open with DEXTER

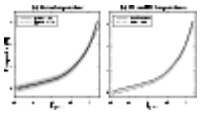

Figure 4: a) Average temperature stratification in the penumbra (solid). The penumbral model of TTR (shifted by 200 K) is also shown for comparison (dashed). The shaded areas represent the rms fluctuations of the temperature. **b)** Average temperature stratification in the center-side and limb-side penumbra (solid and dashed, respectively). The error of the mean ($\sigma/\sqrt{N}$) is around 2 K in both cases.

Open with DEXTER

The mean temperature stratification of the penumbra considering all pixels is shown in Fig. 4a. For comparison, we also plot the mean temperature stratification obtained by TTR. The two curves have the same curvature at all heights, but are shifted by 200 K (our temperatures being cooler than those of TTR). We do not deem that the offset of 200 K is significant, as different spots may certainly show different temperatures. In addition, the two data sets may be affected by different levels of stray light contamination.

In Fig. 4b we plot the average temperature stratifications for the center-side and limb-side penumbra. Again, the curvature of the two stratifications is very similar, but the limb-side penumbra is inferred to be cooler than the center-side penumbra at all heights. The difference is larger in the upper layers (up to 150 K). A similar asymmetry has been reported by Rouppe van der Voort (2002) from an analysis of Ca II K observations. Rouppe van der Voort suggests that the larger average temperature of the center-side penumbra is produced by an excess of bright structures in the outer penumbra. Our results support this idea. In Fig. 5, histograms of the temperature at $\log \tau_{500} = 0$ are presented for the inner and outer parts of the penumbra. The inner penumbra does not show significant differences between the two sides of the spot. Pixels in the outer penumbra, by contrast, are generally hotter on the center side.

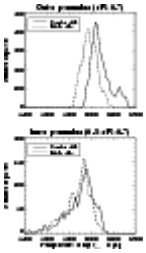

Figure 5: Histograms of temperature at $\log \tau_{500} = 0$ in the outer (*top*) and inner (*bottom*) center-side and limb-side penumbra (solid and dashed lines, respectively).

Open with DEXTER

The fact that different temperatures are inferred in the two sides of the penumbra must be related to the different viewing angle. Indeed, it is difficult to imagine a physical mechanism that could heat the penumbra asymmetrically. Rouppe van der Voort (2002) suggests that the higher temperatures derived in the outer center-side penumbra can be explained by isotherms being tilted downwards away from the umbra. The required tilt is opposite to what one would expect from the Wilson depression (inclined upwards away from the umbra, e.g., Mathew et al. 2004), but it may be real: it has been demonstrated that penumbral flux tubes dive down below the solar surface in the mid penumbra and beyond (Westendorp Plaza et al. 1997, 2001; Bellot Rubio et al. 2004; Borrero et al. 2004). That is, the field lines are slightly inclined downwards in the outer penumbra. Perhaps this configuration of the magnetic field is capable of determining the inclination of the isotherms, although the exact mechanism has not been identified yet.

As pointed out by Rouppe van der Voort (2002), other authors also find that the center-side penumbra is apparently hotter than the limb-side penumbra (e.g., TTR, Westendorp Plaza et al. 2001). To the best of our knowledge, only one discrepant analysis exists. Schmidt & Fritz (2004) have studied the azimuthal variation of the continuum intensity in a number of spots observed at different heliocentric angles. These authors found larger intensities in the limb-side penumbra for spots close to the solar limb, i.e., the opposite behavior. Clearly, more observations are required to settle the issue.

Taking advantage of the high spatial resolution of our data set, we conclude this section with a discussion of the temperature fluctuations observed at different optical depths. Figure 6 displays such fluctuations along an azimuthal path crossing the penumbra at a normalized radial distance of 0.8, for $\log \tau_{500} = 0$, -1, and -2. The fluctuations become smaller and smaller as the upper layers are approached. At $\log \tau_{500} = 0$, the temperature fluctuates by some 200 K, while at $\log \tau_{500} = -2$ the fluctuations are smaller than 50-100 K. The vertical lines mark a few positions where the temperature is enhanced locally. Clearly, hot structures in the deep layers remain hot in the upper layers, but with lower temperature contrasts. This is in excellent agreement with the findings of Rouppe van der Voort (2002) and Bello González et al. (2005). Our results suggest that the structures giving rise to the bright penumbral filaments seen in white-light images (probably flux tubes) are located mainly in the lower photosphere. The small temperature fluctuations observed in high layers do not necessarily imply that flux tubes are present there: if the deep-lying tubes are hot, it is very likely that they can heat the layers above them. Thus, small temperature fluctuations in high layers could be produced by tubes located deeper down.

3.2 Kinematic structure

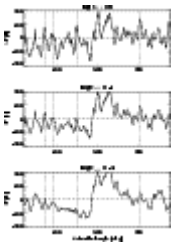

Figure 6: Temperature fluctuations at different optical depths along an azimuthal path at $r/R = 0.8$. The vertical dotted lines mark a number of selected positions showing enhanced temperatures. Azimuthal angles are measured counterclockwise, with $90°$ pointing to the limb and $270°$ to disk center.

Open with DEXTER

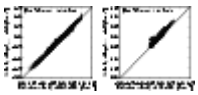

Figure 7: Comparison of LOS velocities resulting from the inversion and bisector velocities at intensity levels of 60%-80% (*left*) and 2%-20% (*right*). The solid lines represent a one-to-one correspondence.

Open with DEXTER

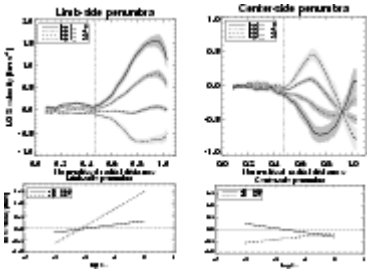

Figure 8: *Top*: radial variation of the azimuthally averaged LOS velocity in the limb-side *(left)* and center-side penumbra *(right)*, for four different optical depths. The shaded areas represent the rms variation of the LOS velocities at each radial distance. Positive LOS velocities indicate motions away from the observer (i.e., redshifts). *Bottom*: average LOS velocity stratifications in the limb-side penumbra (*left*) and center-side penumbra (*right*) at r=0.6R and r=0.97R.

Open with DEXTER

We start this section by examining how well the bisector velocities of Papers I and II compare with the velocities inferred from the inversion. Such a comparison is important to strengthen the conclusions drawn in Paper II from the analysis of the observed bisectors. Figure 7 shows scatter plots of the LOS velocities deduced from the two different methods. As can be seen, the agreement is very satisfactory in both deep and high layers. Bisector velocities near the continuum (intensity levels 60%-80%) are well correlated with the LOS velocities determined at $\log\tau_{500} = -0.6$, with an rms difference of only 55 m s^{-1}. Bisector velocities near the line core (intensity levels 2%-20%) are also well correlated with the LOS velocities returned by the inversion at $\log\tau_{500} \sim -1.8$, the rms difference being about 70 m s^{-1}. We have chosen the optical depths that yield the best agreement, but it should be remarked that they coincide almost exactly with the centroids of the Response Functions (RFs) to velocity perturbations, evaluated in the average penumbral model atmosphere. The centroids are located at $\log\tau_{500} \sim -0.8$ and $\sim$-1.6 for intensity levels of 60%-80% and 2%-20%, respectively. The agreement is not surprising: Ruiz Cobo & del Toro Iniesta (1994) and Sánchez Almeida et al. (1996) have shown that physical parameters measured from spectral lines using simple techniques (e.g., Doppler velocities from line bisectors) are an average of the actual stratification of the parameter weighted by the corresponding RF. If the stratification is linear with depth, then the height of formation of the measured parameter is the centroid of the RF (del Toro Iniesta 2003).

Figure 7 demonstrates that Doppler velocities derived from bisectors near the line core should be ascribed to layers significantly deeper than the "formation height" of the line core. This is because of the very large widths of the RFs of I to $v_{\rm LOS}$. Such widths imply that a wide range of layers contribute to the observed Doppler shift. As shown in Fig. A.1, the line core reacts only little to mass motions in the upper photosphere, so velocities there are difficult to detect unless the contribution of deeper layers is properly considered.

3.2.1 Height variation of the LOS velocity

In Fig. 8 we show the azimuthally averaged LOS velocity at four optical depths as a function of normalized radial distance, for the limb-side and center-side penumbra (left and right upper panels, respectively). The curves depicted in Fig. 8 confirm in a more quantitative way the impression from Fig. 1 that the Evershed flow strongly decreases with height. A velocity reversal is observed around $\log\tau_{500} = -2$. On the limb side, we infer redshifts in the deep photosphere and blueshifts in the upper layers. For most of the center-side penumbra, blueshifts in deep layers and redshifts in high layers are retrieved (an exception is the very outer part of the

center-side penumbra). Interestingly, the LOS velocity stratifications displayed in Fig. 4 of TTR also feature sign reversals around $\log \tau_{500} = -2$. A possible explanation for this reversal is offered in Sect. 4.2.

The lower panels of Fig. 8 show the average velocity stratifications at two radial distances: r=0.6R and r=0.97R. On the limb side, the gradient of $v_{\rm LOS}$ with $\log \tau_{500}$ is significantly larger in the outer penumbra. On the center side, the situation is reversed, with slightly larger gradients in the inner penumbra. These gradients reproduce the slopes of the bisectors observed in the different parts of the penumbra (Fig. 1 of Paper II). Note the occurrence of negative velocities (blueshifts) in the upper layers except in the inner center-side penumbra, where positive velocities are retrieved above $\log \tau_{500} = -2$.

The inferred velocity stratifications, together with the various broadening and smearing mechanisms, explain the line-core blueshifts observed almost everywhere in the penumbra, as well as the small line-core redshifts detected in the inner center-side penumbra (e.g., bisectors #33 and #34 in Paper II). We stress that the line-core blueshifts *cannot* be due to the chromospheric Evershed flow (e.g., Georgakilas et al. 2003), mainly because it would produce non-negligible Doppler shifts only in the outer center-side penumbra. At this location it would show up as a *redshift*, not as a blueshift.

3.2.2 Flow geometry at different heights

We have computed the flow speed and flow angle at different optical depths from the azimuthal variation of the LOS velocities returned by the inversion code. The calculations have been performed as explained in Sect. 5.4 of Paper I. If one assumes that the flow field is axially symmetric, the azimuthally averaged LOS velocity reflects the vertical flow component, and the amplitude of the azimuthal variation of the LOS velocity reflects the horizontal flow component. Using these components, the mean flow inclination and the absolute flow velocity can be deduced. The results of the analysis are presented in Fig. 9 as a function of normalized radial distance.

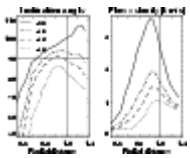

Figure 9: Flow geometry at different optical depths as deduced from the azimuthal variation of the LOS velocity. *Left*: flow inclination (with respect to the local vertical). Inclinations of 90° correspond to horizontal flows. *Right*: absolute magnitude of the flow.

Open with DEXTER

As mentioned in Appendix B, our simple model atmosphere does not account for the possibility of unresolved structure in the resolution element. Thus, the flow speeds resulting from the calculations are probably smaller than the real ones[*]. To first order, however, the flow angles are not influenced by this effect, because they are derived from the *ratio* of the horizontal and vertical components of the flow, and both are affected equally by the lack of spatial resolution. From Fig. 9 we note the following features:

1. the flow inclination (with respect to the local vertical) increases with optical depth. Downflows are present in the mid and outer penumbra, but only in deep layers. In high layers, the flow is always inclined upwards;
2. the flow velocity decreases with decreasing optical depth;
3. the radial position of the maximum flow velocity "migrates" outwards as we go to higher atmospheric layers.

In summary, the *azimuthally averaged* flow velocity increases with depth and the *azimuthally averaged* flow inclination show downflows only in the deep layers. This strengthens the conclusions of Paper II, where we inferred a similar flow configuration from the interpretation of individual bisector shapes. It is important to

remark that calculations using the bisector velocities derived in Paper I lead to the very same flow angles and flow speeds (cf. Fig. 6 in Bellot Rubio 2004), as could have been expected from Fig. 7.

The results presented in Fig. 9 are in good agreement with the flow inclinations determined by Bellot Rubio et al. (2003, 2004) from a two-component inversion of infrared Stokes profiles. The radial variation of the flow angle described by Bellot Rubio et al. corresponds roughly to our curve for $\log \tau_{500} = 0$, because the Fe I 1565 nm lines they use are sensitive to velocities in very deep and narrow photospheric layers. Our results are also consistent with those of Sánchez Cuberes et al. (2005), who inverted spectropolarimetric measurements of a sunspot at disk center in terms of one-component model atmospheres with gradients of velocity. These authors found that downflows occur predominantly in deep layers ($\log \tau_{500} \geq -1$), disappearing higher up in the atmosphere. The present analysis, however, does not confirm the small downflows retrieved by Sánchez Cuberes et al. (2005) in the inner penumbra.

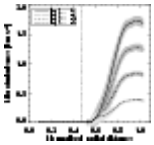

Figure 10: Radial variation of the azimuthally averaged microturbulence at four optical depths. The shaded areas represent the standard deviation of the microturbulent velocities found at each radial distance. The vertical line marks the inner penumbral boundary.

3.2.3 Microturbulence

For each pixel the inversion returns the height variation of the microturbulence, assumed to be linear with $\log \tau_{500}$. Figure 10 shows the azimuthally averaged microturbulence at four optical depths versus normalized radial distance. From this figure it is apparent that:

1. in the inner penumbra, up to about 0.6 penumbral radii, the microturbulence is zero at all heights;
2. in the mid and outer penumbra, the microturbulence is different from zero and increases with optical depth and radial distance;
3. the gradient with depth of the microturbulence increases with increasing radial distance.

In Paper I (Fig. 7) we determined the radial dependence of the azimuthally averaged equivalent width (EW) and the full width at half maximum (FWHM) of the intensity profiles observed in NOAA 10019. For both parameters we found minima in the inner penumbra ($r \sim 0.65R$) and maxima in the outer penumbra ($r \sim 0.95R$). According to the present results, this radial increase of the EW and the FWHM is due to a microturbulence that increases radially (item 2 above).

What is the origin of the microturbulent velocities returned by the inversion code? One can speculate that stronger Evershed flows result in increased shear at the boundary layer separating the flow channels from the surrounding (static) magnetic atmosphere. Strong shears may produce small-scale turbulence through the onset of instabilities. This would explain why we detect enhanced microturbulence in the deep layers of the mid and outer penumbra, where the flow speeds are larger.

However, we also found in Paper I that both the EW and the FWHM tend to be slightly enhanced in the regions of maximum Doppler shifts (i.e., along the line connecting the disk center and the sunspot center). A similar tendency is observed for the microturbulence. Figure 11 shows the microturbulence at $\log \tau_{500} = -1.5$ versus the LOS velocity at the same optical depth. From this figure, it is clear that large LOS velocities are always associated with large microturbulences. The findings of Paper I led us to conjecture that the increase in the EW and the FWHM associated with large velocities may be due to the presence of strongly Doppler-shifted (but

spectrally unresolved) line satellites. If this is indeed the case, then part of the microturbulence we infer may not represent real small-scale turbulence, but a convenient means to account for the effects of line satellites.

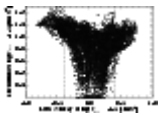

Figure 11: Microturbulence at $\log \tau_{500} = -1.5$ as a function of the LOS velocity inferred from the inversion at the same optical depth. The vertical dotted lines indicate LOS velocities of ± 0.4 km s^{-1}. Larger velocities are always associated with enhanced microturbulence. The same correlation is seen in deeper layers, but less clearly.

Open with DEXTER

4 Discussion

4.1 Origin of enhanced line-wing intensities in the inner penumbra

From an analysis of the Stokes profiles of the Fe I 1564.8 nm line, Bellot Rubio (2003) found that the intensity emerging from the inner penumbra is higher than that emerging from the outer penumbra at wavelengths close to, but not exactly at, the line center. That is, sunspots exhibit a bright ring in the inner penumbra when observed in the wing of spectral lines. The bright ring can be interpreted as a temperature enhancement in the mid-photospheric layers (as it is detected in the wings of the line but not in the continuum or line core).

Our high spatial resolution observations of NOAA 10019 confirm the existence of such a bright ring (Fig. 8 of Paper I) and add new information on it: the intensity enhancement occurs in the form of radial, narrow fibrils very similar to the bright penumbral filaments seen in continuum images, but with much higher contrast (Fig. 3 of Paper I). Moreover, the enhancement is observed preferentially in the inner center-side penumbra blueward of the line core, and in the inner limb-side penumbra redward of the line core. The temperature stratifications of Fig. 3 indicate that the inner penumbra is always cooler than the outer penumbra at all heights in the atmosphere, so the enhanced brightness cannot be due to a temperature effect. Heating of the mid photosphere was the mechanism originally proposed by Bellot Rubio (2003). It is also the scenario favored by Sánchez Cuberes et al. (2005).

Here we argue that the bright ring is actually produced by (a) the small Doppler shifts and line asymmetries observed in the inner penumbra, together with (b) the increase of the line width towards the outer sunspot boundary. The left panel of Fig. 12 shows an intensity map of the spot at $\Delta\lambda = -6.4$ pm from line center (filtergram #42 in Fig. 3 of Paper I). The enhanced brightness of the inner center-side penumbra is apparent in this image. The intensity profiles emerging from the two spatial positions marked with crosses are displayed in the right panel of Fig. 12. As can be seen, these profiles possess very different properties: in the outer penumbra (solid line) they are broader and have a stronger asymmetry than in the inner penumbra (dashed line). The bright ring results from a comparison of the intensities emerging from the inner and outer penumbra at fixed wavelengths. Consider, for example, wavelengths in the blue wing (leftmost vertical line). At this wavelength, the inner penumbra is clearly brighter than the outer penumbra. In the red wing (rightmost vertical line), the inner penumbra would still be brighter, but with a much reduced contrast. This is consistent with the observations described in Paper I. Similar arguments apply to profiles emerging from the limb-side penumbra: because of the smaller line widths and asymmetries in the inner penumbra, the intensity at fixed wavelengths is enhanced relative to the outer penumbra, with higher contrasts redward of the line core.

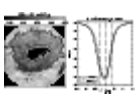

Figure 12: *Left*: intensity map of the spot at $\Delta\lambda = -6.4$ pm from line center. Two pixels belonging to the inner and outer center-side penumbra are marked with crosses. *Right*: best-fit intensity profiles returned by the inversion at the spatial positions marked with crosses in the left panel. Solid: outer penumbra. Dashed: inner penumbra. The vertical dotted lines mark fixed wavelength positions in the blue wing, the line core, and the red wing (*from left to right*). The blue and red wing positions correspond to filtergrams #42 and #58 of Fig. 3 in Paper I.

Thus, the bright ring can be explained satisfactorily in terms of the radial variation of the microturbulence and the Evershed flow. Microturbulence is an important parameter: if it were the same everywhere across the spot, redward of the line core the inner penumbra would appear *darker* than the outer penumbra on the center side, contradicting the observations. To further support the idea that the bright ring is not due to temperature enhancements, we have carried out the same inversions by forcing the LOS velocity to be constant with height (i.e., we do not allow for line asymmetries). Additionally, we set the microturbulence to zero. The temperature maps resulting from these inversions show a bright ring at $\log \tau_{500} = -1$ and no changes in the thermal structure of the deep photospheric layers.

Using flowless maps, Balasubramaniam (2002) detected bright structures in the inner penumbra at wavelengths close to line center (his Fig. 8). Transforming observed intensities into radiation temperatures, he concluded that these structures are hotter than their surroundings. In our opinion, however, they more likely trace regions of reduced Evershed flows and small-scale turbulence.

4.2 Interpretation of the LOS velocity stratifications

In Paper II we demonstrated that the uncombed model proposed by Solanki & Montavon (1993) is able to explain the bisector shapes observed in the penumbra of NOAA 10019. In an uncombed penumbra, the Evershed flow occurs along nearly horizontal flux tubes embedded in a background atmosphere at rest. Here we use this model to interpret the LOS velocity stratifications displayed in Fig. 8.

As pointed out in Appendix B, it is the magnitude and slope of the inferred velocity stratification which inform us about the flow geometry (flow speed and flow angle) and height of the Evershed channels. Figure 5 of Paper II shows that, in the very outer penumbra, two flow channels stacked along the LOS and with different inclination angles are necessary to understand the kinks and reversals of the observed bisectors. In the inner and mid penumbra the bisectors are rather linear, and can be explained in terms of a single, deep-lying flow channel.

Based on these results, in the inner penumbra (r=0.6R) we consider a flow channel located in deep layers, between $\log \tau_{500} = -0.7$ and 0. The flow has a speed of 8 km s^{-1} and an inclination of $87°$ with respect to the vertical. In the outer penumbra (r=0.97R), we assume two flow channels located in deep and mid photospheric layers. The deep-lying channel extends from $\log \tau_{500} = -0.2$ to 0.5. It has a flow speed of 8 km s^{-1} and an inclination of 135°. The upper channel extends from $\log \tau_{500} = -1.8$ to -1.1 and carries an Evershed flow of 7 km s^{-1} making an angle of 85° to the vertical. This flow configuration is similar to the one deduced in Paper II, except for the fact that our higher-lying channel points upwards by 5° instead of being completely horizontal. The LOS velocities resulting from the two flux-tube geometries at the heliocentric angle of our observations ($\theta = 23°$) are represented by solid lines in Fig. 13, for the center and limb-side penumbra.

To investigate whether or not these flow configurations can explain the LOS velocities retrieved from the inversion, we have computed synthetic profiles under the assumption that the resolution element contains two different atmospheres. Their temperature and pressure stratifications are taken to be the mean stratifications deduced from the inversion of NOAA 10019. The LOS velocity is set to zero in the first component, whereas for the second component we use the stratifications of Fig. 13. In the inner penumbra we adopt a filling factor of 0.2, i.e., only 20% of the resolution element is occupied by flows. In the outer penumbra the filling factor is 0.5, as in Paper II. The resulting profiles are convolved with the instrumental profile of TESOS and a macroturbulent velocity of 2 km s^{-1} (inner penumbra) or 1 km s^{-1} (outer penumbra). Finally, they are inverted under the same conditions as the real data (two nodes for velocity, temperature and microturbulence, and a height-independent macroturbulence). It is important to remark that the simulated profiles show the same bisector shapes and bisector variations across the penumbra as the real observations.

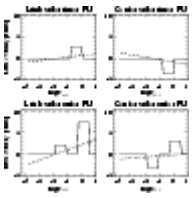

Figure 13: LOS velocity stratifications due to flux tubes embedded in a background atmosphere at rest (solid lines) that produce *linear* velocity stratifications (dashed lines) when two nodes are used to retrieve the actual velocity stratification. See text for details on the flux-tube geometries adopted in the inner and outer penumbra.

Open with DEXTER

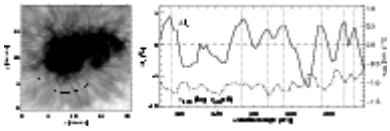

Figure 14: Continuum intensity fluctuations (*solid*) and LOS velocity at $\log \tau_{500} = 0$ (*dashed*) along an azimuthal path crossing the inner center-side penumbra as indicated on the left image. Negative velocities represent blueshifts. The vertical dotted lines mark positions of local maxima of the continuum intensity.

Open with DEXTER

The *linear* velocity stratifications retrieved from the inversion of the simulated profiles are represented by dashed lines in Fig. 13. The first thing to notice is that the inferred stratifications change sign in the mid photosphere (around $\log \tau_{500} = -2$) both on the center and limb sides, even though there are no structures in high layers that could be responsible for such velocity reversals. Actually, the sign reversal is the result of extrapolating the jump(s) of velocity generated by the tubes to the upper layers, where the response of the line to plasma motions is small. This extrapolation effect was first described by Martínez Pillet (2000) in connection with inversions of visible lines that do not account for the existence of penumbral flux tubes. The same effect has been observed by Mathew et al. (2003) in their one-component inversions of infrared lines.

The second thing to note is that the general trends of the LOS velocities inferred from the inversion of NOAA 10019 (lower panels of Fig. 8) are well reproduced by the *linear* velocity stratifications resulting from the flux tube configurations of Fig. 13, although the magnitudes are different. An exact correspondence cannot be expected, given the simplicity of our flux-tube model and the relatively large number of unknown parameters that need to be specified. Trends that are well reproduced include the following:

- on the limb side, the slope of the stratifications is larger in the outer penumbra as compared with the inner penumbra;
- on the center side, the slope of the stratifications is slightly larger in the inner penumbra;
- the LOS velocities corresponding to the outer center-side penumbra are negative all along the photosphere.

This experiment demonstrates that the presence of flux tubes in the penumbra can explain the inversion results. In particular, the unexpected depth dependence of the velocity in the center-side penumbra at normalized radial distances larger than 0.9 (with zero or small redshifts at $\log \tau_{500} = 0$ and blueshifts increasing with height, see Fig. 8) can be understood in terms of two flux tubes stacked along the LOS. The tube lying deeper contributes with positive velocity (i.e., a *redshift*). This redshift is necessary to explain the bisector reversals described in Paper II. In order to produce a redshift in the center-side penumbra, the deep-lying flux tube must be inclined downwards with respect to the horizontal by more than 23° (the heliocentric angle of the spot), otherwise it would show negative velocities and the slope of the resulting LOS velocity stratification would be opposite to what we observe. Flux tubes returning to the solar surface have previously been inferred by, among others, Westendorp Plaza et al. (1997, 2001), Schlichenmaier & Schmidt (2000), Bellot Rubio et al. (2003, 2004) and Borrero et al. (2004, 2005).

The tube located higher in the atmosphere may be horizontal as in Paper II or slightly inclined upwards (by less than 23° from the horizontal). The latter configuration would still produce redshifts on the limb side and blueshifts on the center side, exactly what is required to explain the velocity stratifications observed in the penumbra. Interestingly, such high-lying tubes do not seem to be necessary in the inner penumbra, only in the mid and outer penumbra. It is tempting to associate them with those described by Westendorp Plaza et al. (2001) and Bellot Rubio et al. (2004). These authors found indications of a new family of penumbral tubes in the mid penumbra and beyond. Spectropolarimetric measurements suggest that such tubes are more vertically oriented than the deeper ones, carrying a fraction of the Evershed flow to the upper photosphere.

4.3 Do we see individual flow channels?

Continuum intensity fluctuations and LOS velocities are very well correlated in the inner penumbra. This is shown in Fig. 14, where we plot normalized continuum intensity variations and LOS velocities at $\log \tau_{500} = 0$ along an azimuthal path crossing 8 distinct filaments of the inner center-side penumbra (we do not consider the limb-side part of the azimuthal path because no clear filaments are observed there). The curves depicted in Fig. 14 reveal that *larger continuum intensities are associated with larger LOS velocities*, i.e., the Evershed flow is more intense in the brighter structures, at least in the inner center-side penumbra. This agrees with the conclusions of Bello González et al. (2005) and Schlichenmaier et al. (2005).

However, the most important fact demonstrated by Fig. 14 is that the dark structures also show large LOS velocities. Stray light from the bright filaments may change the line profile in the dark structures, but only to some extent (cf. Sect. 3.2 of Paper I). Unless the stray light contamination is unreasonably large, the velocities found in the dark filaments must be real. This means that we see the Evershed flow everywhere: even at a resolution of $0\farcs5$, there is almost no position in the penumbra where the velocity drops to zero (except where it must be zero for geometrical reasons). In our opinion, this well established fact (see also Hirzberger & Kneer 2001; and Rouppe van der Voort 2002) has not been emphasized adequately in the past.

Since Evershed flows exist in both bright and dark filaments, it is tempting to think that these structures represent individual flow channels (i.e., isolated flux tubes) with different properties. If so, the basic building blocks of the penumbra would have been identified. But this interpretation is problematic. For example, one would have to explain why the flow channels possess different temperatures and velocities at the same radial distance and, more importantly, why there exists such a regular azimuthal pattern of temperature enhancements/coolings and larger/smaller plasma flows. An alternative explanation is that the bright and dark filaments seen in high resolution continuum images are not individual flow channels, but a collection of them. If the filling factor of the tubes changes regularly in the azimuthal direction, i.e., if the number of flow channels present in the resolution element changes azimuthally, then one would observe larger LOS velocities and higher temperatures at those positions where there are more tubes (provided, of course, that the tubes are hot in the inner penumbra, as suggested by the simulations of Schlichenmaier et al. 1998; and the uncombed inversions of Borrero et al. 2005). The important idea here is that the intrinsic flow speed and temperature of the flux tubes would not change azimuthally at a fixed radial distance from sunspot's center, only the filling factor would change. We believe this is a natural explanation for the correlation displayed in Fig. 14. Independent support for this idea has been gathered from the analysis of full Stokes profiles of near-infrared lines (Bellot Rubio 2004; Bellot Rubio et al. 2004).

Our results strongly suggest that the filaments observed in Doppler maps at a resolution of about $0\farcs5$ are still unresolved. That is, they are not individual flow channels. For this reason, in Paper II we referred to them as *flow filaments*, to clearly distinguish them from the actual, smaller flow channels. Recent observations with the Swedish 1-m Solar Telescope (Rouppe van der Voort et al. 2004) also suggest that, even at a resolution of $0\farcs1$, some penumbral filaments may not be resolved.

5 Summary

Using high spectral and spatial resolution intensity profiles of the non-magnetic Fe I 557.6 nm line, we have studied the thermal and kinematic properties of a sunspot at 23° from disk center. The profiles, obtained with TESOS, have been inverted in terms of a one-component model atmosphere with gradients of the physical quantities.

The temperature, LOS velocity, and microturbulent velocity maps resulting from the inversion show that the fine structure of the penumbra is less apparent in high layers than in deep layers. This suggests that the physical mechanism(s) producing the penumbral filaments operate mainly in the lower photosphere.

As others before, we observe higher continuum intensities in the center-side penumbra as compared with the limb-side penumbra. Our analysis thus produces an apparent asymmetry in the inferred temperatures, the center side being hotter by 100-150 K on average. This is most likely due to line-of-sight effects, but further investigation is needed.

We have also investigated the origin of the enhanced line-wing intensities exhibited by sunspots in the inner penumbra. Our results indicate that the bright ring is produced by the smaller line asymmetries and line widths observed in the inner penumbra as compared with the outer penumbra. Thus, it does not reflect temperature enhancements in the mid photosphere.

The inferred LOS velocities have been used to determine the geometry of the Evershed flow assuming axial symmetry of the flow field. We find that both the flow speed and flow angle increase with optical depth and radial distance. Downflows are detected in the mid and outer penumbra, but only in deep layers ($\log \tau_{500} \geq -1.4$). By means of simulated profiles, we have shown that the velocity stratifications retrieved from the inversion are consistent with the existence of penumbral flux tubes channeling the Evershed flow. In the inner penumbra, a deep-lying tube slightly inclined upwards is able to explain the observations. In the outer penumbra, two flux tubes stacked along the LOS and with different inclination angles are necessary. The deep-lying tube is inclined downwards, whereas the higher-lying tube carries upflows. We suggest that the latter may belong to a different family of tubes, perhaps the ones first described by Westendorp Plaza et al. (2001).

Finally, we have demonstrated that there is an excellent correlation between continuum intensities and LOS velocities in the inner center-side penumbra, with larger Evershed flows associated with brighter continuum structures. Very remarkably, however, dark structures also exhibit significant Evershed flows. This led us to propose that the bright and dark filaments seen in continuum images at a resolution of $0\farcs5$ are not individual flow channels, but a collection of them.

Our analysis shows that spectroscopy with 2D filter instruments provides a wealth of information on the physical properties of sunspots. Obviously, the next step is to carry out 2D spectropolarimetric observations near the diffraction limit. This will soon be possible with instruments like the Interferometric BIdimensional Spectrometer (IBIS) and the KIS/IAA Visible Imaging Polarimeter (VIP) attached to TESOS.

Acknowledgements

We thank D. Soltau, T. Berkefeld and T. Schelenz for developing the KAOS system. T. Berkefeld operated KAOS during our observations. T. Kentischer built, upgraded, programmed, and aligned TESOS. The constructive criticism of an anonymous referee helped us to improve an earlier version of the manuscript. This work has been supported by the Spanish MCyT under *Programa Ramón y Cajal* and project ESP2003-07735-C04-03, and by the German DFG under grants SCHL 514/2-1 and PE 782/4. The German Vacuum Tower Telescope is operated by the Kiepenheuer-Institut für Sonnenphysik on the Spanish Observatorio del Teide of the Instituto de Astrofísica de Canarias.

References

- Balasubramaniam, K. S. 2002, ApJ, 575, 553 [NASA ADS] [CrossRef] (In the text)

- Barklem, P. S., Piskunov, N., & O'Mara, B. J. 2000, A&AS, 142, 467 [EDP Sciences] [NASA ADS] (In the text)
- Bello González, N., Okunev, O. V., Domínguez Cerdeña, I., Kneer, F., & Puschmann, K. G. 2005, A&A, 434, 317 [EDP Sciences] [NASA ADS] [CrossRef] (In the text)
- Bellot Rubio, L. R. 2003, ASP Conf. Ser., 307, 301 [NASA ADS] (In the text)
- Bellot Rubio, L. R. 2004, Rev. Mod. Astron., 17, 21 (In the text)
- Bellot Rubio, L. R., Balthasar, H., Collados, M., & Schlichenmaier, R. 2003, A&A, 403, L47 [EDP Sciences] [NASA ADS] [CrossRef] (In the text)
- Bellot Rubio, L. R., Balthasar, H., & Collados, M. 2004, A&A, 427, 319 [EDP Sciences] [NASA ADS] [CrossRef] (In the text)
- Borrero, J. M., Solanki, S. K., Bellot Rubio, L. R., Lagg, A., & Mathew, S. K. 2004, A&A, 422, 1093 [EDP Sciences] [NASA ADS] [CrossRef] (In the text)
- Borrero, J. M., Lagg, A., Solanki, S. K., & Collados, M. 2005, A&A, 436, 333 [EDP Sciences] [NASA ADS] [CrossRef] (In the text)
- Cabrera Solana, D., Bellot Rubio, L. R., & del Toro Iniesta, J. C. 2005, A&A, 439, 687 [EDP Sciences] [NASA ADS] [CrossRef] (In the text)
- del Toro Iniesta, J. C. 2003, Introduction to Spectropolarimetry (Cambridge: Cambridge University Press) (In the text)
- del Toro Iniesta, J. C., Tarbell, T. D., & Ruiz Cobo, B. 1994, ApJ, 436, 400 [NASA ADS] [CrossRef] (TTR) (In the text)
- Georgakilas, A. A., Christopoulou, E. B., Skodras, A., & Koutchmy, S. 2003, A&A, 403, 1123 [EDP Sciences] [NASA ADS] [CrossRef] (In the text)
- Gray, D. F. 1988, The observation and analysis of stellar photospheres (New York: Wiley) (In the text)
- Hirzberger, J., & Kneer, F. 2001, A&A, 378, 2001 (In the text)
- Kentischer, T. J., Schmidt, W., Sigwarth, M., & Uexkuell, M. V. 1998, A&A, 340, 569 [NASA ADS] (In the text)
- Maltby, P. 1964, Astrophysica Norvegica, 8, 205 [NASA ADS] (In the text)
- Martínez Pillet, V. 2000, A&A, 361, 734 [NASA ADS] (In the text)
- Mathew, S. K., Lagg, A., Solanki, S. K., et al. 2003, A&A, 410, 695 [EDP Sciences] [NASA ADS] [CrossRef] (In the text)
- Mathew, S. K., Solanki, S. K., Lagg, A., et al. 2004, A&A, 422, 693 [EDP Sciences] [NASA ADS] [CrossRef] (In the text)
- Rimmele, T. R. 1995, A&A, 298, 260 [NASA ADS] (In the text)
- Rouppe van der Voort, L. H. M. 2002, A&A, 389, 1020 [EDP Sciences] [NASA ADS] [CrossRef] (In the text)
- Rouppe van der Voort, L. H. M., Löfdahl, M. G., Kiselman, D., & Scharmer, G. B. 2004, A&A, 414, 717 [EDP Sciences] [NASA ADS] [CrossRef] (In the text)
- Ruiz Cobo, B., & del Toro Iniesta, J. C. 1992, ApJ, 398, 375 [NASA ADS] [CrossRef] (In the text)
- Ruiz Cobo, B., & del Toro Iniesta, J. C. 1994, A&A, 283, 129 [NASA ADS] (In the text)
- Sánchez Almeida, J., Ruiz Cobo, B., & del Toro Iniesta, J. C. 1996, A&A, 314, 295 [NASA ADS] (In the text)
- Sánchez Cuberes, M., Puschmann, K. G., & Wiehr, E. 2005, A&A, 440, 345 [EDP Sciences] [NASA ADS] [CrossRef] (In the text)
- Scharmer, G. B., Gudiksen, B. V., Kiselman, D., Löfdahl, M. G., & Rouppe van der Voort, L. H. M. 2002, Nature, 420, 151 [NASA ADS] [CrossRef] (In the text)
- Schlichenmaier, R., & Collados, M. 2002, A&A, 381, 668 [EDP Sciences] [NASA ADS] [CrossRef] (In the text)
- Schlichenmaier, R., & Schmidt, W. 2000, A&A, 358, 1122 [NASA ADS] (In the text)
- Schlichenmaier, R., Jahn, K., & Schmidt, H. U. 1998, A&A, 337, 897 [NASA ADS] (In the text)
- Schlichenmaier, R., Bruls, J. H. M. J., & Schüssler, M. 1999, A&A, 349, 961 [NASA ADS] (In the text)
- Schlichenmaier, R., Bellot Rubio, L. R., & Tritschler, A. 2004, A&A, 415 (Paper II) (In the text)
- Schlichenmaier, R., Bellot Rubio, L. R., & Tritschler, A. 2005, Astron. Nachr., 326, 301 [NASA ADS] [CrossRef] (In the text)
- Schmidt, W., & Fritz, G. 2004, A&A, 421, 735 [EDP Sciences] [NASA ADS] [CrossRef] (In the text)
- Solanki, S. K. 2003, A&AR, 11, 153 [NASA ADS] (In the text)
- Solanki, S. K., & Montavon, C. A. P. 1993, A&A, 275, 283 [NASA ADS] (In the text)

- Soltau, D., Berkefeld, T., von der Lühe, O., Wöger, F., & Schelenz, T. 2002, Astron. Nachr., 323, 236 [NASA ADS] [CrossRef] (In the text)
- Thomas, J. H., & Weiss, N. O. 2004, ARA&A, 42, 517 [NASA ADS] (In the text)
- Tritschler, A., Schlichenmaier, R., Bellot Rubio, L. R., & the KAOS Team 2004, A&A, 415, 717 [EDP Sciences] [NASA ADS] [CrossRef] (Paper I) (In the text)
- Tritschler, A., Schmidt, W., Langhans, K., & Kentischer, T. J. 2002, Solar Phys., 211, 17 [NASA ADS] [CrossRef] (In the text)
- von der Lühe, O., Soltau, D., Berkefeld, T., & Schelenz, T. 2003, SPIE, 4853, 187 [NASA ADS] (In the text)
- Westendorp Plaza, C., del Toro Iniesta, J. C., Ruiz Cobo, B., et al. 1997, Nature, 389, 47 [NASA ADS] [CrossRef] (In the text)
- Westendorp Plaza, C., del Toro Iniesta, J. C., Ruiz Cobo, B., et al. 2001, ApJ, 547, 1130 [NASA ADS] [CrossRef] (In the text)

Online Material

Appendix A: Properties of Fe I 557.6 nm

In this appendix we examine the diagnostic capabilities of Fe I 557.6 nm in some detail. Fe I 557.6 nm is a non-magnetic photospheric line commonly used for velocity measurements. It is often quoted to be insensitive to temperature, but Fig. 5 of Paper I shows that the equivalent width of Fe I 557.6 nm changes by non-negligible amounts when going from the quiet sun to the umbra, where the temperatures are rather different.

In the following, we elaborate on the temperature sensitivity of Fe I 557.6 nm by means of response functions (RFs, see Ruiz Cobo & del Toro Iniesta 1994; and del Toro Iniesta 2003). The upper panel of Fig. A.1 shows the RF of Fe I 557.6 nm to temperature perturbations as evaluated in the penumbral model atmosphere of del Toro Iniesta et al. (1994, hereafter TTR). This plot tells us how much the specific intensity at λ changes when the temperature of the model is increased by 1 K at a given optical depth τ_{500}. The figure demonstrates that the line reacts to temperature changes. The sensitivity of any spectral line to temperature perturbations is determined by two competing effects: changes in the absorption and in the source function. Usually, only opacity variations are considered (e.g., Gray 1988, Chap. 13) but, as pointed out by Cabrera Solana et al. (2005), the *dominant* contribution is that of the source function. Neglect of this dominant factor is the likely cause of the line being quoted as temperature insensitive in most publications.

Figure A.2 shows the temperature dependence of the equivalent width for a set of neutral iron lines commonly used in solar physics (adapted from Cabrera Solana et al. 2005). It is apparent from this figure that Fe I 557.6 nm is one of the most temperature sensitive lines. Indeed, it shows a larger sensitivity than lines presumed to be appropriate for temperature measurements such as Fe I 524.7 and 525.0 nm. The large variation of the equivalent width of Fe I 557.6 nm with temperature is consistent with the observed behavior of the line in the quiet sun, umbra and penumbra (Fig. 5 of Paper I).

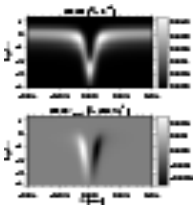

Figure A.1: Response functions of the Fe I 557.6 nm line to temperature *(top)* and line-of-sight velocity *(bottom)*. The two plots indicate the percentage by which the specific intensity at λ changes when the temperature (resp. LOS velocity) is increased by 1 K (resp. 1 m s^{-1}) in a layer of optical width $\Delta \log \tau_{500} = 0.1$ and optical depth τ_{500}. The thermal stratification of the penumbral model of TTR has been employed for these calculations.

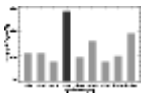

Figure A.2: Variation of the equivalent width W of 9 neutral iron lines when the temperature is increased by 1 K in all photospheric layers. The calculations have been carried out using the thermal stratification of the penumbral model of TTR.

Let us now turn our attention to the sensitivity of Fe I 557.6 nm to line-of-sight (LOS) velocities. The bottom panel of Fig. A.1 shows the RF of the intensity to velocity perturbations as evaluated in the penumbral model of TTR. These RFs correspond to a model where all velocities have been set to zero, so they are symmetric about the line center (models in which the LOS velocity varies with height would result in asymmetrical RFs and slightly different sensitivities in the different atmospheric layers). As can be seen, the line is sensitive to velocities in a height range from about $\log \tau_{500} = 0$ to -3.5. The maximum sensitivity is attained in the mid photosphere. In the deep and high layers where the continuum and the line core are formed, respectively, the sensitivity to velocities is much reduced. The reason has been explained by Cabrera Solana et al. (2005): at a given wavelength, the intensity variation induced by Doppler shifts is proportional to the *slope* of the line at that position. Thus, the intensity changes are maximum near the line wings (which sample the mid photosphere) and minimum near the continuum and the line core, where the slope of the intensity profile ($dI/d\lambda$) quickly goes to zero. The lower panel of Fig. A.1 also demonstrates that the intensity observed at a fixed wavelength is sensitive to LOS velocities in a broad range of optical depths. That is, the Doppler shifts measured from line bisectors at a given intensity level contain information from a significant fraction of the atmosphere. Thus, it is difficult to ascribe them to any particular layer. This limitation of bisector analyses has long been recognized (Maltby 1964; Rimmele 1995).

Appendix B: Model atmosphere and inversion

As mentioned in Sect. 2, we have adopted a one-component model atmosphere with gradients of the physical parameters to invert the Fe I 557.6 nm profiles observed with TESOS. Here we provide the reader with more information about the advantages and limitations of the model. We also give examples of best-fit profiles resulting from the inversion, which has been performed using a parallelized version of the SIR code in a 16-processor Linux Beowulf cluster. The time needed to invert the full data set is about 2.5 h.

Without additional spectral lines observed, or measurements of the four Stokes parameters, it is not possible to estimate the amount of stray light contamination. We expect, however, that stray light arising from seeing fluctuations is much reduced with respect to earlier observations that did not benefit from adaptive optics. By contrast, parasitic light inside TESOS has been corrected for. In Paper I we determined that $\sim 5\%$ of the mean continuum intensity contributes to each filtergram in the form of ghosts and scattered light. This parasitic light has been subtracted from the individual images before extracting the intensity profiles.

Our inversion approach avoids important shortcomings of simpler analyses. Since the complete radiative transfer problem is solved, we effectively separate the contribution of temperatures and LOS velocities to the observed profiles using the information provided by the RFs. From Fig. A.1 it is clear that the intensity at a fixed wavelength depends on the temperature and LOS velocity stratification along the atmosphere. Thus, we determine both parameters simultaneously in order not to misinterpret thermal effects as velocity effects and vice versa. Another important improvement is that we can ascribe the inferred velocities and temperatures to specific optical depths, because our procedure takes into account the finite width of the intensity contribution functions.

The simple one-component model atmosphere used in this work has several limitations. First, it does not allow for any unresolved structure in the pixel. Although our spatial resolution is one of the highest ever reached in spectroscopic studies, we are still far from resolving the individual constituents of the penumbra. Spectropolarimetric measurements suggest that the penumbra is *uncombed*, i.e., that it consists of nearly horizontal magnetic flux tubes embedded in a more vertical background field (Solanki & Montavon 1993;

Schlichenmaier & Collados 2002; Bellot Rubio et al. 2003, 2004; Borrero et al. 2004, 2005, and references therein). The flux tubes carry most of the Evershed flow, while the background atmosphere is essentially at rest. If the flux tubes and the background are horizontally unresolved and we do not account for this possibility, the LOS velocities determined from the inversion would represent *lower* limits to the real velocities. Second, we have chosen a very simple functional dependence to describe the run of the LOS velocity with height. In an uncombed penumbra, lines of sight that pierce the tubes would "see" discontinuities in the LOS velocity as they encounter the upper and lower boundaries of the tubes. Our assumption of linear velocity stratifications would provide only a very rough description of such discontinuous velocity stratifications. In that case, it would be the magnitude and sign of the LOS velocity gradient inferred from the inversion which would inform us about the velocity inside the flux tubes and the height position of the flow channels.

Despite these shortcomings, the adopted model atmosphere does an excellent job in explaining the observed intensity profiles. On average, the residuals of the fit are only slightly largerthan the noise (after 2×2 binning, the observed profiles have a signal-to-noise ratio of about 120 in the continuum intensity). Figure B.1 shows examples of profiles recorded in the center- and limb-side penumbra, along with the best-fit profiles resulting from the inversion. The very asymmetrical shapes induced by the photospheric Evershed flow are successfully reproduced, indicating that the assumption of linear LOS velocity stratifications suffices to explain the observed Doppler shifts and line bisectors. This is true for all profiles showing linear bisectors. In the very outer penumbra, bisector kinks and reversals are common (Paper II). We cannot reproduce these profiles so well, although the fits are still reasonably good (cf. Fig. B.2). In these cases, it seems that more complex LOS velocity stratifications than the one used here would apply.

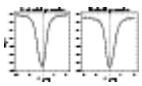

Figure B.1: Examples of observed (dots) and best-fit (solid lines) intensity profiles emerging from the center-side *(left)* and limb-side *(right)* penumbra. The vertical dashed lines indicate the position of zero velocities (see Paper I). Note the strong asymmetries of the line, with an extended blue wing in the center-side penumbra and an extended red wing in the limb-side penumbra.

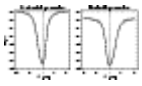

Figure B.2: Same as Fig. B.1, for profiles in the outer penumbra showing bisector kinks and reversals. These profiles are not so well fitted in terms of a one-component model with linear LOS velocity stratifications.